

Direct Observation of the Local Microenvironment in Inhomogeneous CO₂ Reduction Gas Diffusion Electrodes via Versatile pOH Imaging

Annette Boehme^{1,2}, Justin C. Bui^{3,4}, Aidan Fenwick^{2,5}, Rohit Bhide⁶, Cassidy N. Feltenberger^{6,7}, Alexandra J. Welch^{1,2}, Alex J. King^{3,4}, Alexis T. Bell^{3,4}, Adam Z. Weber⁴, Shane Ardo^{6,7,8,9}, and Harry A. Atwater^{*1,2}

¹Department of Applied Physics and Material Science, California Institute of Technology, Pasadena, CA 91125, USA

²Liquid Sunlight Alliance, California Institute of Technology, Pasadena, CA 91125, USA

³Department of Chemical and Biomolecular Engineering, University of California Berkeley, Berkeley, CA 94730, USA

⁴Liquid Sunlight Alliance, Lawrence Berkeley National Laboratory, Berkeley, CA 94730, USA

⁵Department of Chemistry and Chemical Engineering, California Institute of Technology, Pasadena, CA 91125, USA

⁶Department of Chemistry, University of California Irvine, Irvine, CA 92697, USA

⁷Liquid Sunlight Alliance, University of California Irvine, Irvine, CA 92697, USA

⁸Department of Chemical and Biomolecular Engineering, University of California Irvine, Irvine, CA 92697, USA

⁹Department of Materials Science and Engineering, University of California Irvine, Irvine, CA 92697, USA

S1: Experimental Methods

Materials: Potassium bicarbonate (KHCO₃, 99.95%, Sigma Aldrich), potassium hydroxide (KOH, Macron Fine Chemicals 6984-06), CO₂ gas (Research grade, 99.999%, Airgas), 6,8-dihydroxy-1,3-pyrenedisulfonic acid (DHPDS, ≥97.0%, Sigma Aldrich), 8-Aminopyrene-1,3,6-trisulfonic acid trisodium salt (APTS, ≥96.0%, Sigma Aldrich), Sigracet 22 BB carbon paper (Fuel Cell Store), laminated PTFE membrane filters (pore size 0.1-0.2 μm and 0.45 μm, Sterlitech), copper (99.999%, Plasmaterials), Pt mesh (99.9%, 0.0726 mm diameter wires, Alfa Aesar), leakless Ag/AgCl reference electrode (edaaq ET072). All materials were used without further modification. Deionized water used in all experiments was filtered through a 0.22 μm Millipak Express 40, serial number 0826.

Instruments: AMOD dual electron beam deposition system (System 02520, Angstrom Engineering), NOVA NanoSEM 450 scanning electron microscope confocal with an Oxford Instrument's Xmax 80 mm2, Oakton 5+ pH meter, Denver Instruments Ultra Basic pH meter, Zeiss LSM 710 confocal microscope with a WN Achroplan 63x water immersion objective (numerical aperture 0.9), Biologic SP-200 potentiostat, Masterflex 77120-62 pump, CO₂ gas flow controller (Alicat Scientific, MC-50SCCM-D/5M), SRI-8610 gas chromatograph.

Fabrication of Cu GDEs: Copper gas diffusion electrodes were fabricated by electron-beam deposition of 300 nm copper on Sigracet 22BB carbon paper. For this, an AMOD dual electron beam deposition system (System 02520, Angstrom Engineering) was used. 300 nm of Cu was deposited on the microporous layer of the carbon paper substrate at a rate of 2 Å/s with a rotating substrate holder. The deposited samples were spray-coated, first with a solution of one part deionized water, one part isopropyl alcohol and 2.5 mg carbon black per mL of solution, then with a solution of one part deionized water, one part isopropyl

alcohol and 0.5 mL of 5 weight% Nafion per mL of solution. Both coatings were applied from a distance of eight centimeters for one second. The samples were then dried overnight in vacuum.

Scanning Electron Microscopy (SEM) characterization: A NOVA NanoSEM 450 scanning electron microscope was used to capture images of the samples. The spot size was set to three and the acceleration voltage to 15 kV. To identify if copper is present inside trenches, energy dispersive X-ray spectroscopy (EDS) was performed with an Oxford Instrument's Xmax 80 mm² in the aforementioned SEM with a spot size of five.

Calibration of ratiometric fluorescent dyes: DHPDS and APTS are each ratiometric dyes that report on the local activity of OH⁻, because their spectra exhibit at least two distinct peaks that change in intensity in different directions upon altering the pOH (**Figure S4a** and **b**). The ratio of emission from either dye is determined by calculating the ratio of the signals from both peaks. It is independent of the local dye concentration, within the concentration ranges used in the experiments. To determine calibration curves of the ratio of emission as a function of pOH as shown in **Figure S4c**, aqueous solutions of known pOH were prepared. For this, aqueous stock solutions of KOH and HCl were diluted with nanopure water. The pOH of the solutions was confirmed by measuring the pH separately with two different pH meters (Oakton 5+ and Denver Instruments Ultra Basic pH meter) and calculating the pOH using pOH = 14 – pH. Both pH meters were calibrated with buffer solutions at pH 4, pH 7, and pH 10 before use. In the prepared solutions with known pOH, 100 μM DHPDS or 100 μM APTS was diluted from a stock solution. A laser beam scans the sample solutions line by line over the center of a liquid droplet, which was repeated three times and the average ratio of emission was calculated and correlated with the known pOH. For both dyes, the ratio of emission was plotted as a function of pOH and best fit to a sigmoidal function:

$$\begin{aligned} \text{For DHPDS: } (Ratio\ of\ Emission)_{DHPDS} &= \frac{33.72}{(1 + \exp^{1.413 \cdot (pOH_{DHPDS} - 5.971)})} + 5.571 \rightarrow \\ pOH_{DHPDS} &= 5.917 + \frac{1}{1.413} \ln \left(-1 + \frac{33.72}{(Ratio\ of\ Emission)_{DHPDS} - 5.571} \right) \end{aligned} \quad (S1)$$

$$\begin{aligned} \text{For APTS: } (Ratio\ of\ Emission)_{APTS} &= \frac{5.005}{(1 + \exp^{-2.743 \cdot (pOH_{APTS} - 2.05)})} + 0.1041 \rightarrow \\ pOH_{APTS} &= 2.05 - \frac{1}{2.743} \ln \left(-1 + \frac{5.005}{(Ratio\ of\ Emission)_{APTS} - 0.1041} \right) \end{aligned} \quad (S2)$$

In the case of DHPDS, three distinct peaks in the absorption spectra are important for the calibration curve, one for each of the doubly protonated (R-(OH)₂), monoprotinated (R-(OH)(O⁻)), and doubly deprotonated (R-(O⁻)₂) states of the dye in its electronic ground state. Because DHPDS is a strong photoacid (pK_a* ≈ 0), excitation of either protonation state of DHPDS at near-neutral-pH conditions results in emission from a deprotonated form of the thermally equilibrated electronic excited state of the dye. This is because the kinetics for excited-state proton transfer are significantly faster than the excited-state lifetime of the dye and thus the thermally equilibrated electronic excited-state of the dye reaches chemical quasi-equilibrium. Therefore, we excite DHPDS separately using 458 nm laser light (100% maximum power) and 488 nm laser light (20% maximum power) with the pinhole set to 70.1 μm and the gain set to 800 for each channel. Emitted light is detected in the wavelength interval of 505 – 754 nm separately for each excitation wavelength, and thus the emission ratio is the ratio between the signals

collected from the two excitations. That emission ratio data as a function of pOH fits well to the nonideal Henderson–Hasselbalch equation, also known as the Hill equation,

$$(\text{Ratio of Emission}) = \frac{1}{1 + 10^{n(\text{pH} - \text{p}K_{a \text{ obs}}^*)}}, \quad (\text{S3})$$

with n the Hill coefficient ideality factor, $\text{p}K_{a \text{ obs}}^*$ an effective excited-state $\text{p}K_a$, and $\text{pH} = 14 - \text{pOH}$, to obtain the calibration curve.¹ The main contributor to the nonideal behavior of the titration data is likely the two $\text{p}K_a$ values for DHPDS, which is well supported by the observation of two isosbestic points in the titration data (**Figure S4a**).

In the case of APTS, two distinct peaks in the fluorescence spectra are important for the calibration curve, one for each of the protonated (R-NH_2) and deprotonated (R-NH^-) states of the dye in its thermally equilibrated electronic excited state. Because APTS is a very weak acid ($\text{p}K_a > 14$), deprotonation of its electronic ground state requires $\text{pH} > 14$. Thus, only the protonated electronic ground state of APTS as the aromatic amine can be excited. However, in the presence of a large concentration of OH^- , the thermally equilibrated electronic excited state can be quenched via proton transfer to OH^- to form the deprotonated electronic excited state. Thus, emission can be observed from either protonation state, as the amine (R-NH_2^*) or the aminide (R-NH^-*). As such, we excite APTS using 458 nm laser light (100% power) with the pinhole set to 57.1 μm and the gain set to 800. Emitted light is detected separately in the wavelength intervals of 480 – 550 nm and 551 – 754 nm, and thus the emission ratio is the ratio between the signals collected in the two emission wavelength ranges. That emission ratio data as a function of pH is best fit to the nonideal nonlinear dynamic Stern–Volmer equation and OH^- as the quenching species,

$$(\text{Ratio of Emission}) = \frac{1}{1 + \left((K_{SV, \text{OH}^-}) a_{\text{OH}^-} \right)^n}, \quad (\text{S4})$$

with K_{SV, OH^-} the Stern-Volmer quenching constant, a_{OH^-} the activity of OH^- equals $10^{-\text{pOH}}$, and n and ideality factor, to obtain the near-ideal calibration curve.¹

Stability of ratiometric fluorescent dyes: When performing measurements with the dye DHPDS in the current density range between 0 and -20 mA/cm^2 , no significant decrease in photoluminescence intensity was observed. Some loss of fluorescent signal is observed for cathodic current densities of 100 mA/cm^2 in magnitude, or larger, but in our application the signal of DHPDS saturates for current densities larger in magnitude than 20 mA/cm^2 so this effect is not relevant herein.

However, for APTS we observed a decrease in photoluminescence intensity for current density magnitudes $> 80 \text{ mA}/\text{cm}^2$ and we used APTS to investigate the operation of a GDE with current densities as high as 200 mA/cm^2 in magnitude. To understand this effect, we evaluated the stability of APTS under different conditions (see **Figure S9 (a), (b)**). We observed a decrease in photoluminescence intensity from APTS with and without light and for solutions with pH 7.1 and pH 3, where the degradation effect was more pronounced for the pH 3 solution. Furthermore, we noticed a significant change in color of a 10 mM APTS stock solution that was exposed to -100 mA/cm^2 for 30 minutes, from bright green to brown (see **Figure S9 (c)**), that persisted for days without indication of reverting back to its original form. This suggests an irreversible chemical transformation and not a transient instability, such as formation of an excited-state triplet state or a metastable state. We observe the most significant and irreversible decrease in

photoluminescence intensity from aqueous APTS under the following simultaneous conditions: (i) cathodic current densities $>80 \text{ mA/cm}^2$ in magnitude, and (ii) closer to the electrode surface and/or within trenches. The presence of illumination does not seem to play a role. In addition, we do not think that CO_2R products are resulting in observed degradation, because the steady state photoluminescence spectrum of APTS showed minimal change in intensity as concentration of dissolved inorganic carbon increased (see **Figure S1**). Hence, we suspect that APTS is being reduced at the electrode surface.

Irrespective, calibration curves of fresh APTS solutions with different APTS concentrations, as well as a curve that was measured with an APTS stock solution that was exposed to -100 mA/cm^2 for 5 minutes, are nearly identical (see **Figure S9 (d)**), suggesting that APTS is suitable to use as a pOH sensor even in the presence of significant degradation to a less emissive product. This can be explained by the ratiometric nature of APTS as a pOH sensor.

pOH imaging with confocal microscopy and fluorescent ratiometric dyes: For each of DHPDS and APTS, the dye is dissolved in solution and placed under a Zeiss LSM 710 confocal microscope with a WN Achroplan 63x water immersion objective dipped into the solution. A laser beam scans the sample line by line with the settings described above. For both dyes, the pOH is calculated with the calibration curves obtained in Equations S1 and S2.

Electrochemical cell: The electrochemical cell used for pOH imaging with confocal microscopy was designed to be compatible with the confocal microscope. Because we use a water-immersion objective, the electrolyte chamber must be open at the top. This means that the cell is oriented horizontally, otherwise the electrolyte would spill. The working distance of the water immersion objective is 1.7 mm. In order to allow the objective to be placed this close to the GDE surface, the cell operates without ion-exchange membranes. The cell was 3D-printed, the surfaces were sanded. A rubber gasket is placed in between the bottom gas chamber part and the top electrolyte chamber part for sealing. A hole where the GDE is placed connects the gas- and electrolyte chambers, which is circular and has a surface area of 0.2 cm^2 . For experiments with applied current, a leakless Ag/AgCl reference electrode is used, and a Pt mesh is dipped into the electrolyte as the counter electrode. The electrolyte chamber, including the tubes used for pumping, holds approximately 10 mL of electrolyte when the objective is immersed into it.

pOH imaging experiments without applied current: Experiments to visualize CO_2 diffusion through a porous GDE were performed with the electrochemical cell described above. The pOH was resolved with the dye APTS according to the above explained procedure. 1 M KOH (pOH 0) was chosen as the electrolyte, so an expected increase in pOH upon exposure to CO_2 can be detected with APTS. Experiments were performed with carbon paper GDEs prepared as described above, both at locations with a trench present and at locations without a trench present. In addition, laminated PTFE substrates with different pore sizes, coated with 300 nm Cu in the same way as carbon paper, were investigated. Experiments were carried out both with and without electrolyte flow through two perpendicular inlet tubes at a rate of 6 mL/min. Measurements were performed in the plane perpendicular to the GDE surface by scanning the laser line by line and moving the stage in the z-direction. The measuring speed was adjusted such that capturing one frame takes four to five seconds. The experiment was conducted as a time-series. A CO_2 gas stream of 10 SCCM through the gas chamber along the back of the GDE was turned on after 1 minute of continuous measurements. This time point was later defined as $t = 0 \text{ s}$.

pOH imaging experiments under applied current: Experiments to map the pOH around an operating GDE performing CO_2 reduction were performed with the electrochemical cell and the GDE described above. Aqueous electrolytes of different KHCO_3 concentrations were used (100 mM, 200 mM and 400 mM). Before each experiment, the electrolyte was bubbled with 30 SCCM CO_2 gas for at least 30 minutes. The

pH was monitored with an Oakton 5+ pH meter and bubbling was continued until the pH stabilized. This ensured that the electrolyte was saturated with CO₂. All experiments were conducted with both DHPDS and APTS dyes. The dye was dissolved in the CO₂-saturated electrolyte: DHPDS at a concentration of 100 μM to investigate current densities smaller in magnitude than -20 mA/cm², APTS at a concentration of 200 μM for 100 mM KHCO₃ electrolyte/ 300 μM for 200mM and 400 mM KHCO₃ electrolyte, to investigate current densities larger in magnitude than -20 mA/cm². The electrochemical cell was assembled with a Cu GDE, Ag/AgCl leakless reference electrode and Pt mesh counter electrode. The cell was placed under the confocal microscope and the electrolyte chamber was filled with the prepared electrolyte. All experiments were conducted with electrolyte flow (6 mL/min through two perpendicular inlets) and with a gas stream of 10 SCCM CO₂ through the gas chamber of the electrochemical cell. To determine the series resistance of the cell filled with electrolyte, potentiostatic electrochemical impedance spectroscopy (PEIS) was performed before each experiment with a Biologic SP-200 potentiostat. This allowed us to perform an 85% IR electronic compensation of the electrochemical potential. A trench that is approximately 20 μm wide was identified on the GDE surface. The stage was positioned such that the focal point of the objective was 20 μm below the GDE surface inside the trench. A constant current was applied with the potentiostat. Measuring under galvanostatic conditions enables a constant flux of ions between electrodes. The system was allowed to reach steady state for 15 seconds, then a frame was captured in the x-y plane as described above. The speed was set to three such that taking one image takes approximately 45 seconds. The same procedure was repeated for the focal point being at the GDE surface and 20 μm above the surface for various different current densities. In between each measurement, the electrolyte was removed and replaced to introduce fresh, unused dye. All measurements were conducted at least three times.

Product detection: An electrochemical cell optimized for use with gas chromatography was used for product detection during the performance of CO₂R experiments with copper on carbon paper GDEs. A leakless Ag/AgCl electrode served as reference electrode and a platinum mesh as counter electrode. An anion exchange membrane (AGC, Selemion AMV) was used to separate cathode and anode. The gas chamber takes the form of a serpentine channel at the back of the GDE. The cell was sonicated before each experiment for at least 40 minutes and rinsed thoroughly after each experiment. 100 mM KHCO₃ saturated with CO₂ was pumped through the catholyte and anolyte chambers at a rate of 6.3 mL/min. CO₂ was fed into the gas chamber at a rate of 10 SCCM. A flow meter placed before and after the cell was used to ensure that there were no gas leaks. The gas coming from the cell was returned to a electrolyte bath as a precaution in case of electrolyte breakthrough through the GDE. From there, the gas was sent through a vapor trap to an SRI-8610 gas chromatograph. Chronopotentiometry experiments (constant current) were carried out at -10, -50, -100 and -200 mA/cm² with a potentiostat. Before each experiment, potentiostatic electrochemical impedance spectroscopy (PEIS) was carried out to measure the resistance of the cell. This allowed us to compensate the electrochemical potential by 85% with iR compensation.

S2: COMSOL Model Outline

The model domain is presented in **Figure S11**, which considers a single, periodic trench in a gas diffusion electrode (GDE). Steady-state species conservation governs the species transport for dissolved CO₂, OH⁻, H⁺, HCO₃⁻, CO₃²⁻, and K⁺ within the entire model domain,

$$\nabla \cdot N_i = R_{B,i} \quad (S5)$$

where N_i is the flux of species i , and $R_{B,i}$ is a volumetric source term describing generation of species i due to homogeneous buffer reactions. The Nernst-Planck equation is used to calculate the molar flux of species i ,²

$$N_i = -D_i \nabla c_i - \frac{z_i F}{RT} D_i c_i \nabla \phi_L, \quad (S6)$$

where D_i , c_i , z_i are the diffusivity, concentration, and charge of species i , respectively, ϕ_L is the liquid-phase electric potential, F is the Faraday constant, R is the ideal-gas constant, and T is the temperature. The first term captures the transport of species by diffusion, and the second term describes charged species migration, which does not affect uncharged CO_2 .³ The diffusivities are provided in **Table S1**. To solve for the liquid-phase potential, electroneutrality is enforced,

$$\sum_i z_i c_i = 0 \quad (S7)$$

Table S1: List of model diffusivities and their source.

Species	Diffusivity [$\text{m}^2 \text{s}^{-1}$]	Reference
$D_{K^+,w}$	1.957×10^{-9}	4
$D_{H^+,w}$	9.311×10^{-9}	4
$D_{OH^-,w}$	5.293×10^{-9}	4
$D_{HCO_3^-,w}$	1.185×10^{-9}	4
$D_{CO_3^{2-},w}$	9.10×10^{-10}	4
$D_{CO_2,w}$	1.91×10^{-9}	4

The homogeneous bulk reactions captured by the source term, $R_{B,i}$, are



where $k_{n/-n}$ and K_n are the rate constants and equilibrium constant for reaction n , respectively. These constants are provided in **Table S2**. k_{-n} is calculated by

$$k_{-n} = \frac{k_n}{K_n}, \quad (\text{S13})$$

and $R_{B,i}$ is given by^{5,6}

$$R_{B,i} = \sum_n s_{i,n} c_{ref} \left(k_n \prod_{s_{i,n} < 0} a_i^{-s_{i,n}} - \frac{k_n}{K_n} \prod_{s_{i,n} > 0} a_i^{s_{i,n}} \right), \quad (\text{S14})$$

where $s_{i,n}$ is the stoichiometric coefficient for species i in reaction n , and a_i is the activity of species i . c_{ref} is a reference concentration defined as 1 M. Although it is well-established that Reaction S8 involves two elementary reaction steps with an H_2CO_3 intermediate, we omit them from the model, as is commonly done, because intermediate concentrations are very small and inconsequential to simulation results. In this regard, K_3 and k_3 are overall observed equilibrium and rate constants, respectively.

Table S2: List of buffer reaction constants and their source.

Reaction	Constant ^a	Unit	Ref.
K_1	4.27×10^{-7}	–	7
k_1	0.0371	s^{-1}	7
K_2	4.58×10^{-11}	mol L^{-1}	7
k_2	59.44	s^{-1}	7
K_3	4.27×10^7	L mol^{-1}	7
k_3	2.23×10^3	$\text{L mol}^{-1} \text{s}^{-1}$	7
K_4	4.86×10^3	–	7
k_4	6.9×10^9	$\text{L mol}^{-1} \text{s}^{-1}$	7
K_w	1×10^{-14}	mol L^{-1}	7
k_w	1.4×10^{-3}	$\text{mol L}^{-1} \text{s}^{-1}$	7

^aThe forward rate constants were scaled by a factor of 0.2 to achieve electrolyte buffering more reflective of the experimental results. This minor scaling is reasonable given the large degree of reported rate constants.

The boundary conditions at the edge of the mass-transport boundary layer are Dirichlet boundary conditions, defined by the equilibrium concentrations of a KHCO_3 electrolyte saturated with CO_2 . The boundary layer thickness employed is 200 μm thick, consistent with prior research in similar flow cells⁷, and recent work in this area that have done full CFD simulations of electrochemical CO_2 reduction cells have shown that within the boundary layer, electrolyte convection is not important due to the no-slip boundary condition at the electrode surface.¹² The key mode of transport in the boundary layer is ionic diffusion, which dictates the local pH at the surface and in the trench and is captured adequately by the present model. Moreover, the liquid-phase potential is set to zero. At the left and right boundaries, periodic boundary conditions are employed, where “ n ” is the normal vector.

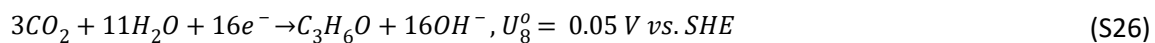
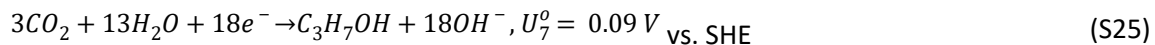
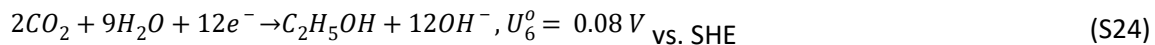
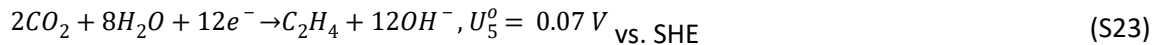
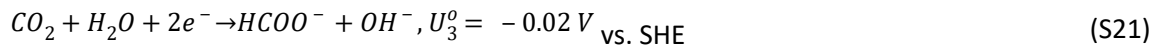
$$\phi_L^{\text{right}} = \phi_L^{\text{left}} \quad (\text{S15})$$

$$c_i^{\text{right}} = c_i^{\text{left}} \quad (\text{S16})$$

$$-n \cdot N_i^{\text{right}} = n \cdot N_i^{\text{left}} \quad (\text{S17})$$

$$-n \cdot \nabla \phi_L^{\text{right}} = n \cdot \nabla \phi_L^{\text{left}} \quad (\text{S18})$$

This boundary condition simulates the periodicity of the trenches in the GDE. At the Cu surface, we specify the CO_2 concentration to be 34 mM, since CO_2 gas is being fed from the backside and dissolving into the electrolyte next to the Cu surface. This boundary condition is of course a simplification, and assumes no gaseous CO_2 transport losses within the gas diffusion layer, which will not hold at higher current densities. However, modeling gaseous phase CO_2 transport in the gas diffusion layer is beyond the scope of the present study, which is primarily focused on transport of OH^- anions and dissolved CO_2 reacting at the electrode surface. In addition, the following electrochemical reactions are assumed to occur:



To capture the formation of H_2 , C_1 (CO , HCOO^- , and CH_4), and C_{2+} (C_2H_4 , $\text{C}_2\text{H}_5\text{OH}$, $\text{C}_3\text{H}_7\text{OH}$, and $\text{C}_3\text{H}_6\text{O}$) products on Cu in the model, Neumann boundary conditions are specified by a concentration-dependent Tafel expression, equation S27, and Faraday’s law, equation S28,

$$i_k = -i_{o,k} \left(\frac{c_{CO_2}}{c_{ref}} \right)^{\gamma_{CO_2,k}} \exp(-\gamma_{pH,k,SHE} pH) \exp\left(-\frac{\alpha_{c,k} F}{RT} (\phi_s - \phi_l - U_{0,k})\right) \quad (S27)$$

$$N_k = -\frac{\nu_k i_k}{nF} \quad (S28)$$

where $\gamma_{CO_2,k}$ is the CO₂ reaction order, $\gamma_{pH,k}$ is the sensitivity of the current density to pH, ϕ_s is the solid phase electrode potential, ϕ_l is the liquid phase electrolyte potential, and $i_{o,k}$, $\alpha_{c,k}$, $U_{0,k}$, and ν_k are the exchange current density, transfer coefficient, equilibrium potential, and reaction stoichiometric coefficient for product k , respectively. Moreover, n is the number of electrons transferred in the electrochemical reaction. $\gamma_{CO_2,k}$ are taken from fits of experimental data from CO₂ and CO reduction at varied partial pressure as discussed in our prior study by Weng *et al.*⁸⁻¹⁰ $\gamma_{pH,k,SHE}$ are taken from fits of experimental data for partial current vs. pH at a constant potential on an SHE scale,^{9,11} wherein HCOOH, H₂ and CH₄ have been observed to have pH dependent kinetics.^{5,12-15} $i_{o,k}$ and α_c are fit to the experimental data collected in this study for dark electrolysis on a Cu GDE in 1 M KHCO₃ and take into account the fit rate orders for CO₂ and pH. The fitted rate parameters are provided in **Table S3**, and the agreement with our experimental GDE data is shown in **Figure S12**.

Notably, the effect of cations has been highly studied in recent CO₂ reduction literature on Cu electrodes. While important, because the same cation is used throughout all experiments (K⁺), these effects will be implicitly captured in the fit exchange current densities¹⁶, as recent work has shown that beyond the type of cation employed, the concentration of the cation is not as important in dictating the electrochemical performance due to the saturation of cations in the OHP of the Cu double layer.¹⁷ Nonetheless, future experimental and simulation work should be employed to more thoroughly probe and understand the impact of cations in the double layer on CO₂R performance to further advance understanding of the kinetics of this reaction on Cu.

Lastly, while it is known that *CO coverage is a major defining factor in the performance of CO₂R at high overpotentials, fully accounting for *CO coverage effects would require the implementation of a microkinetics model, which requires far deeper understanding of the mechanism of CO₂R on Cu, beyond the scope of the present work. We note that the lack of consideration of *CO coverage effects could also potentially explain the discrepancy between the modeled and observed product distributions at 200 mA/cm², wherein the model overpredicts the formation of CO and underpredicts the formation of HCOOH. Nonetheless, the model still replicates the trends very well at all other current densities, and future work should seek to address the effects of coverage and expand the understanding of microenvironment on CO₂R activity at higher current densities.

Table S3: Final kinetic parameters for modeling CO₂ reduction on a Cu GDE in 1 M KHCO₃.

Product	$i_{o,k}$ (mA cm ⁻²)	$\alpha_{c,k}$	$\gamma_{CO_2,k}$	$\gamma_{pH,k,SHE}$
H ₂	3.84 x 10 ⁻³	0.23	0	0.40
CO	1.10 x 10 ⁻³	0.3	1.50	0
HCOO ⁻	2.13 x 10 ²	0.4	2.00	1.56
C ₂ H ₄	9.91 x 10 ⁻⁸	0.40	1.36	0
C ₂ H ₅ OH	8.14 x 10 ⁻¹⁰	0.43	0.96	0
CH ₄	6.80 x 10 ⁻⁴	0.5	0.84	1.56

S3: Computational Methods

The governing equations (electrolyte species material balances and electroneutrality) were used within the Tertiary Current Distribution Module and were solved with the MUMPS general solver in COMSOL Multiphysics 6.0 with a relative tolerance of 0.001. The modeling domain was discretized with a uniform square mesh and was comprised of 20284 elements. A sensitivity analysis on the mesh size was performed, and the results were found to be independent for meshes greater than the 1000 elements required to achieve convergence at low current densities, but higher current densities required 20000 elements or more.

S4: Calculation of Geometric Current Density

To compare simulation to experiment, the simulation current densities, which are averaged to the electrochemically active surface area, must be rescaled to the geometric area. To do so, the following expression is used to approximate this conversion:

$$i_{Geo} = i_{ECSA} \times \frac{L_1 + L_2}{200 \mu m} \quad (S29)$$

where L_1 and L_2 are labelled in **Figure S11**. Using this expression assumes that the geometry of a single, periodic trench domain is characteristic of the geometry of the entire cracked GDE, where in actuality the geometry will consist of a distribution of trenches of varying width and height. Nonetheless, accounting for the true geometry would require employing a high-fidelity pore-network model or a direct numerical simulation of the entire 3D porous electrode, both of which are beyond the scope of the present work.

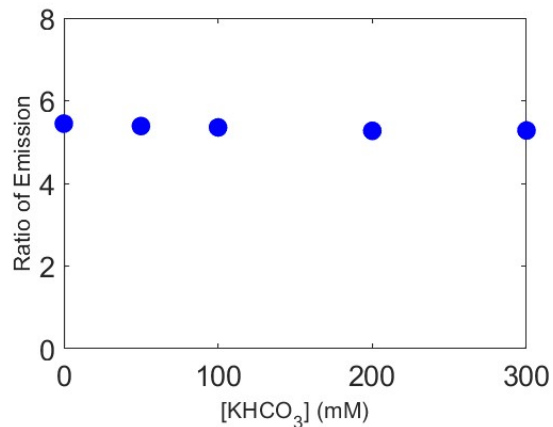


Figure S1: Ratio of Emission of APTS as a function of KHCO_3 concentration. The experiment was carried out in an ammonia buffer solution to keep the pOH constant (it varied by less than 0.1 pOH units). The total amount of ionic charge was kept constant for all data points by adding NaCl to the test solutions. The ratio of emission from APTS is nearly independent of KHCO_3 concentration, indicating that aqueous dissolved inorganic carbon species insignificantly influence the sensing mechanism of APTS.

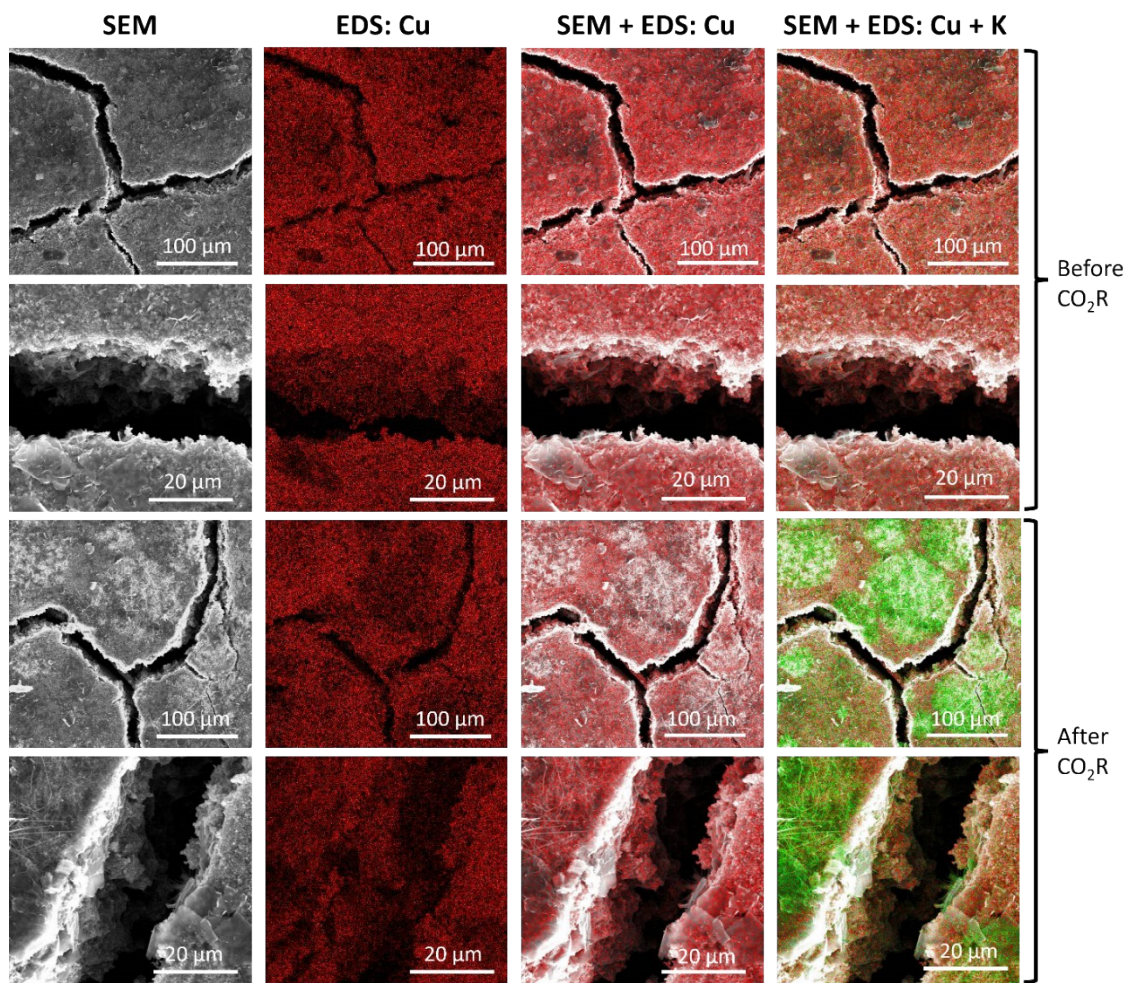


Figure S2: SEM and EDS maps of trenches in a copper GDE surface, before and after CO₂R experiments. First column: SEM images. Second column: EDS maps of the same area with red color signaling the presence of copper. Third column: Overlay of SEM and EDS maps of copper. This shows that copper is present on trench walls and at the bottom of trenches with a similar morphology and appearance before and after CO₂R. Forth column: Overlay of SEM and EDS maps of copper (red) and potassium (green). No potassium is present before CO₂R experiments, but there are potassium deposits on samples after CO₂R experiments that originate from the KHCO₃ electrolyte.

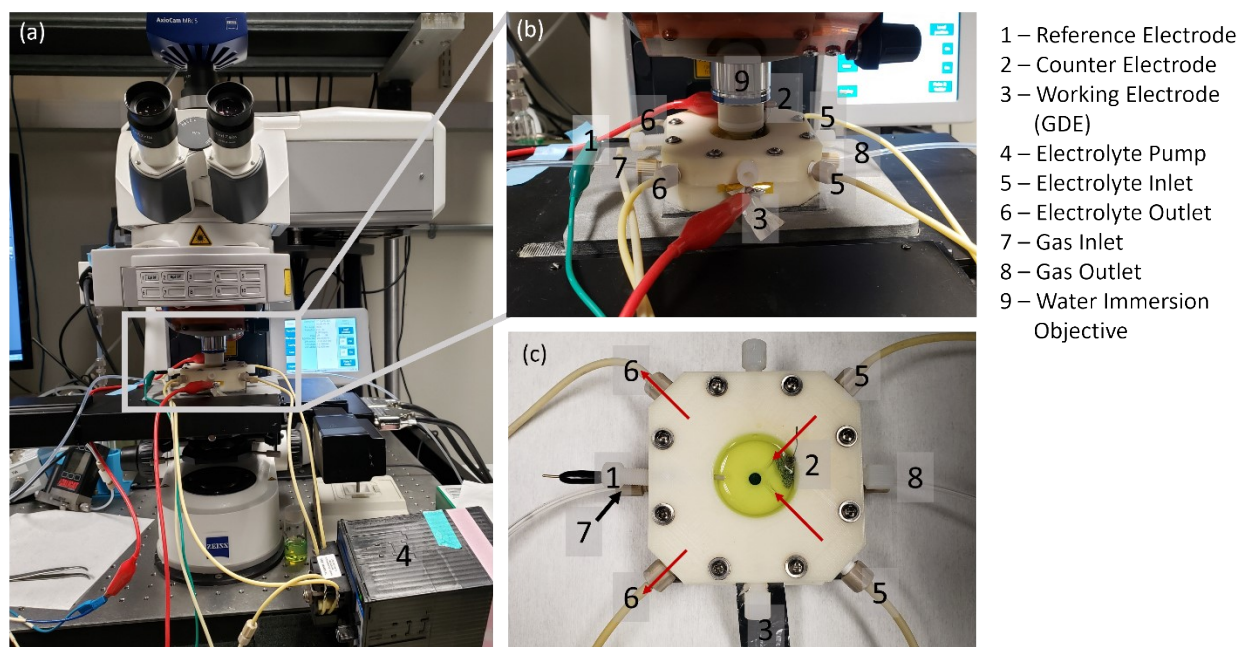


Figure S3: Photographs of the imaging setup with labels. **(a)** Electrochemical flow cell placed under a Zeiss LSM 710 confocal microscope with water-immersion objective. **(b)** Close-up image of the cell. **(c)** Top view of the cell filled with electrolyte, showing two perpendicular electrolyte inlets and outlets (marked with arrows).

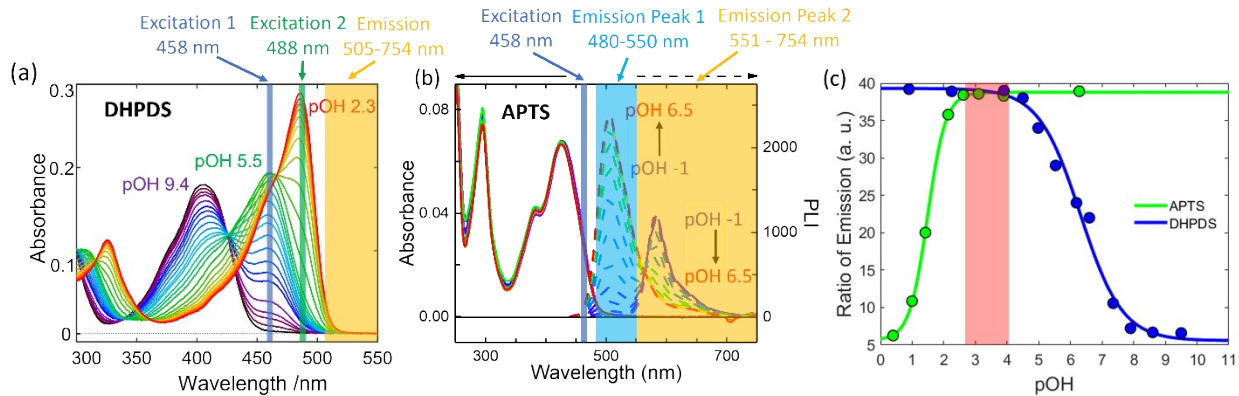


Figure S4: UV-Visible absorption and photoluminescence spectra and calibration curves for the dyes DHPDS and APTS as a function of solution pOH. **(a)** UV-visible absorption spectrum of DHPDS as a function of solution pOH, where the solution pOH was varied between 2.3 and 9.4. The colored regions mark the two excitation wavelengths (458 nm and 488 nm) and the detection range of the fluorescent signal (505 nm – 754 nm) used for ratiometric sensing. **(b)** UV-Visible absorption (solid lines) and photoluminescence (dashed lines) spectra of APTS as a function of solution pOH, where the solution pOH was varied between -1 and 6.5. The colored regions mark the excitation wavelength (458 nm) and two detection wavelength ranges (480 nm – 550 nm and 551 nm – 754 nm) of the fluorescent signal used for ratiometric sensing. **(c)** Calibration curves of both DHPDS (blue) and APTS (green) with the measured ratio of emission as a function of pOH together with best fit curves (Equations S1 and S2). In this plot, the signal for APTS was scaled by $(\text{Ratio of Emission}) \cdot 3 + 5$ for better visibility. The shaded red area indicates the pOH range that cannot be resolved by use of either dye.

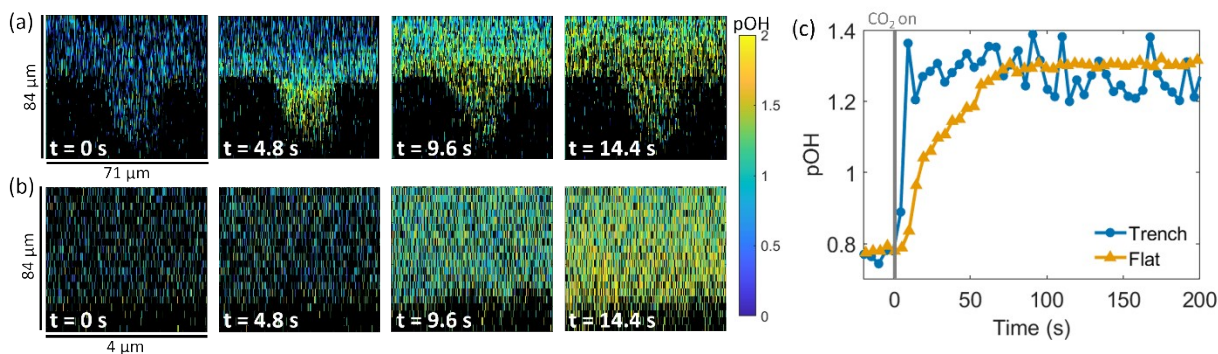


Figure S5: pOH change in the electrolyte due to CO_2 diffusion through a carbon paper GDE **(a)** with a trench, **(b)** without a trench, both without electrolyte flow. Measurements performed with 1M KOH electrolyte with 100 μM APTS, 10 SCCM CO_2 turned on at $t = 0$ s. Panels in **(a)** and **(b)** show pOH maps in the plane perpendicular to the electrode surface for different times. **(c)** Average pOH at a location 20 μm above the surface, showing how it changes as a function of time both with and without a trench. The vertical gray line indicates when the CO_2 flow was turned on.

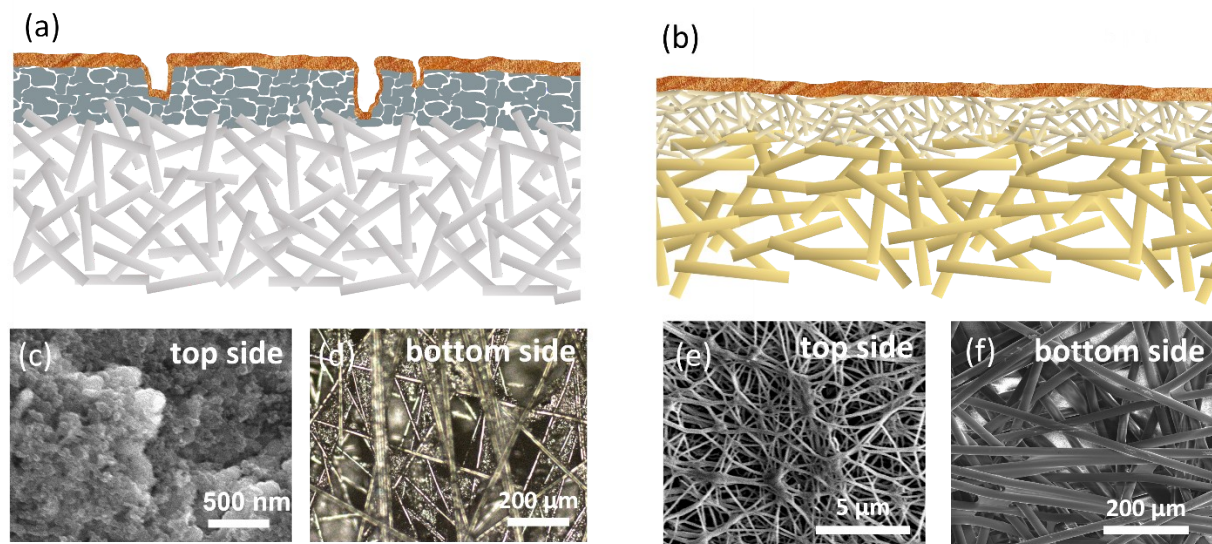


Figure S6: Schematic representations of the structure of a Sigracet 22 BB carbon paper GDE **(a)** and a PTFE membrane GDE (not to scale) **(b)**, both coated with 300 nm Cu, together with SEM images of the top side **(c)** and the bottom side **(d)** of the carbon paper GDE as well as of the top side **(e)** and the bottom side **(f)** of the PTFE GDE.

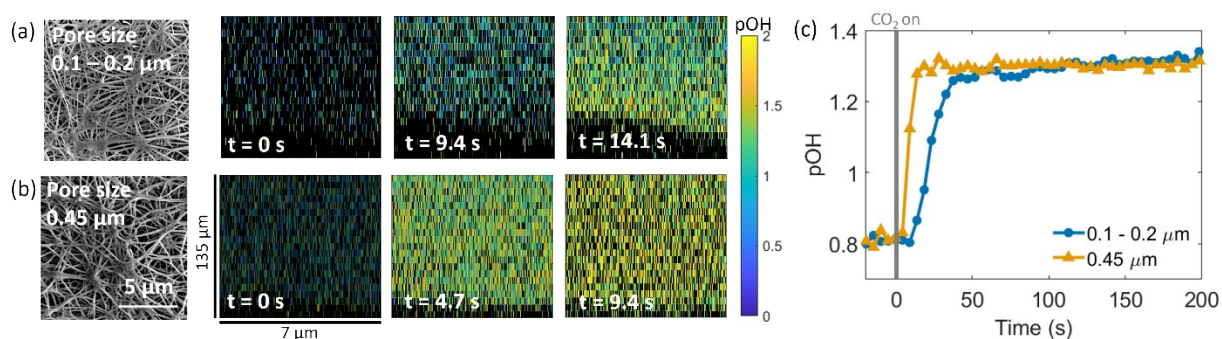


Figure S7: pH change in the electrolyte due to CO_2 diffusion through a PTFE GDE with pore size 0.1-0.2 μm **(a)** and 0.45 μm **(b)**, both without electrolyte flow. Measurements performed in 1 M KOH electrolyte with 100 μM APTS, 10 SCCM CO_2 turned on at $t = 0$ s. Panels in **(a)** and **(b)** show SEM images of the GDE (scale bar applies to both **(a)** and **(b)**) as well as pH maps as a cross section in the plane perpendicular to the electrode surface for different times. **(c)** Change in average pH at a location 20 μm above the surface as a function of time for both GDE substrates with different pore sizes. The vertical gray line indicates when the CO_2 flow was turned on.

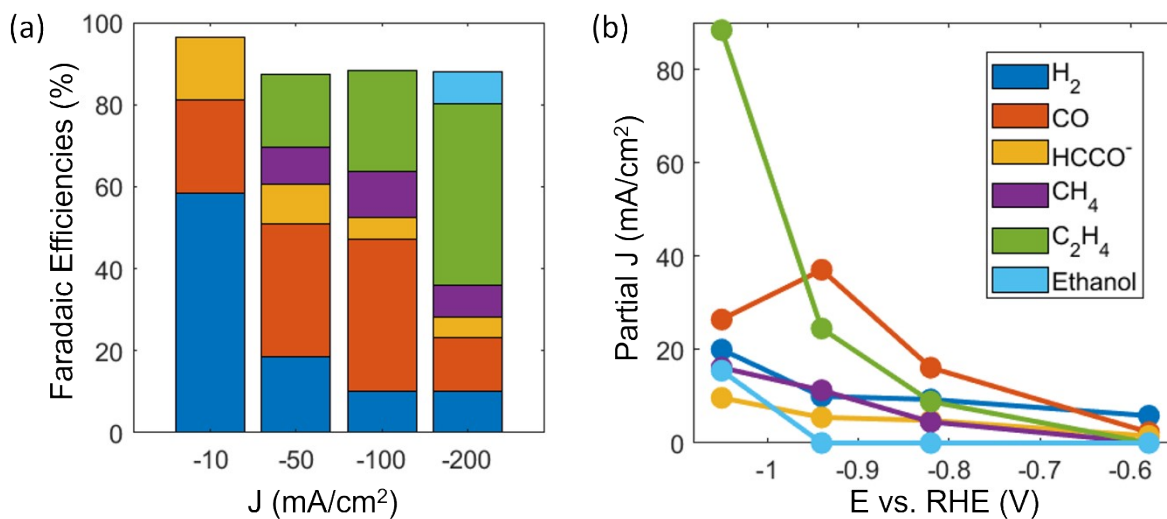


Figure S8: CO₂R performance characterization of 300 nm Cu on carbon paper GDEs. **(a)** Faradaic efficiencies at different current densities. **(b)** Partial current densities for different products as a function of electrode potential vs. the reversible hydrogen electrode. The legend applies to both panels **(a)** and **(b)**.

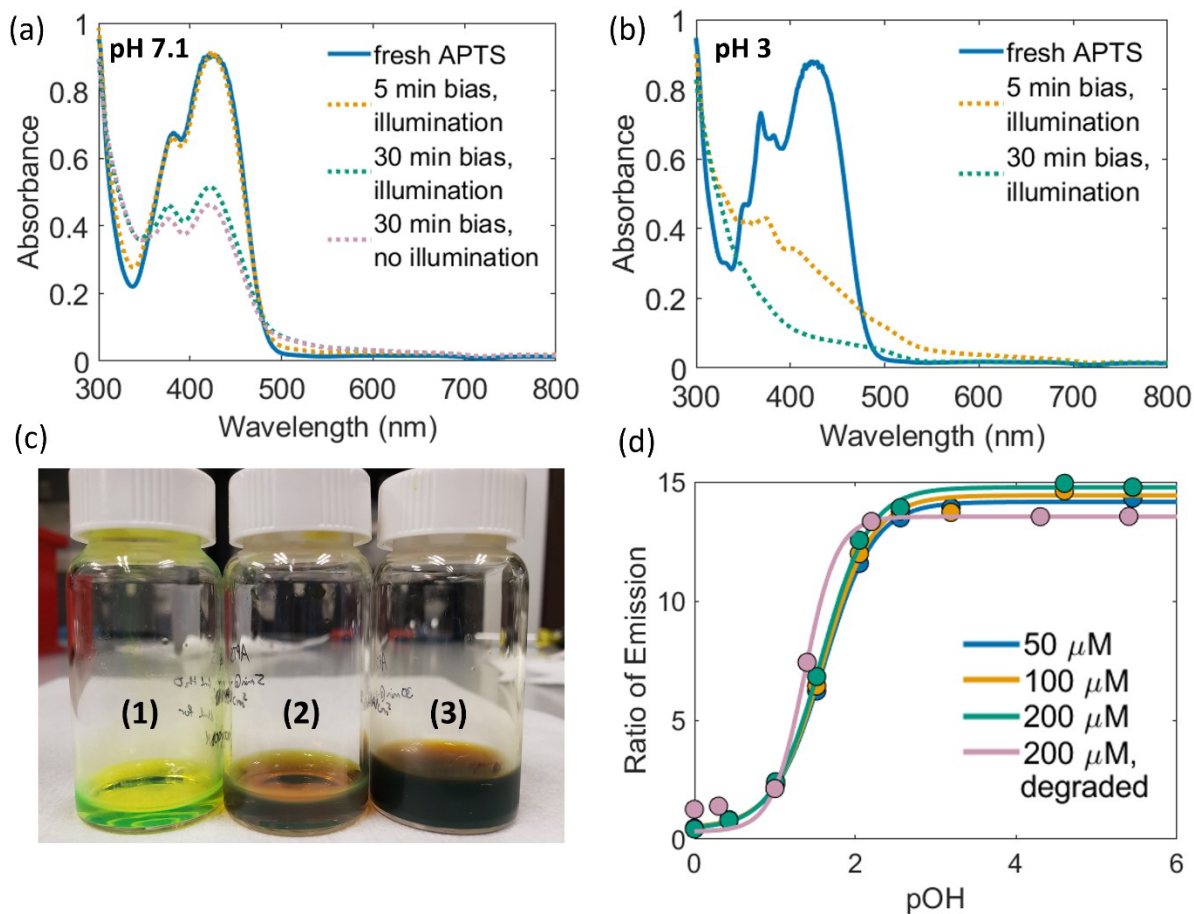


Figure S9: (a) UV-VIS spectra of 200 μM APTS in aqueous 100 mM KHCO_3 , as freshly prepared, and exposed to a GDE operating at -100 mA/cm^2 for 5 minutes under laser illumination, and for 30 minutes, with and without laser illumination. (b) UV-VIS spectra of 200 μM APTS in an aqueous HCl pH 3 solution as freshly prepared and exposed to a GDE operating at -100 mA/cm^2 under laser illumination for 5 minutes and for 30 minutes. (c) Photographs of aqueous 10 mM APTS stock solutions: (1): fresh, (2): degraded by exposure to a GDE operating at -100 mA/cm^2 for 5 minutes, (3): degraded by exposure to a GDE operating at -100 mA/cm^2 for 30 minutes. (d) Calibration curves of APTS with the measured ratio of emission as a function of pOH together with best fit curves for different APTS concentrations between 50 μM and 200 μM and for 200 μM APTS that was degraded by exposure to a GDE operating at -100 mA/cm^2 for 5 minutes (solution (2) in panel (c)).

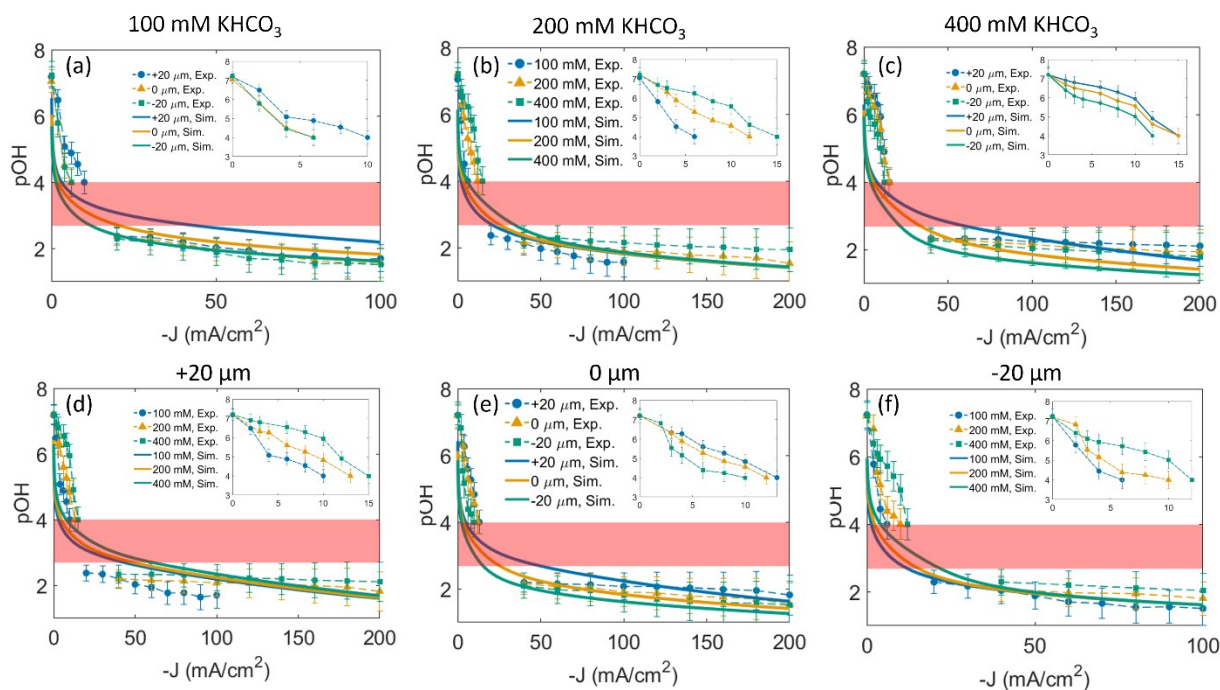


Figure S10: Average pOH as a function of current density, obtained with 100 μM DHPDS ($J \geq -10 \text{ mA}/\text{cm}^2$) and 200/ 300 μM APTS ($J \leq -20 \text{ mA}/\text{cm}^2$). The top row compares the pOH at different positions around a GDE for KHCO_3 concentrations of 100 mM (a), 200 mM (b) and 400 mM (c). The bottom row compares the pOH for different KHCO_3 concentrations at positions around a GDE (d) 20 μm above the surface, (e) at the surface and (f) 20 μm below the surface inside a trench. All panels show both experimental and simulation results.

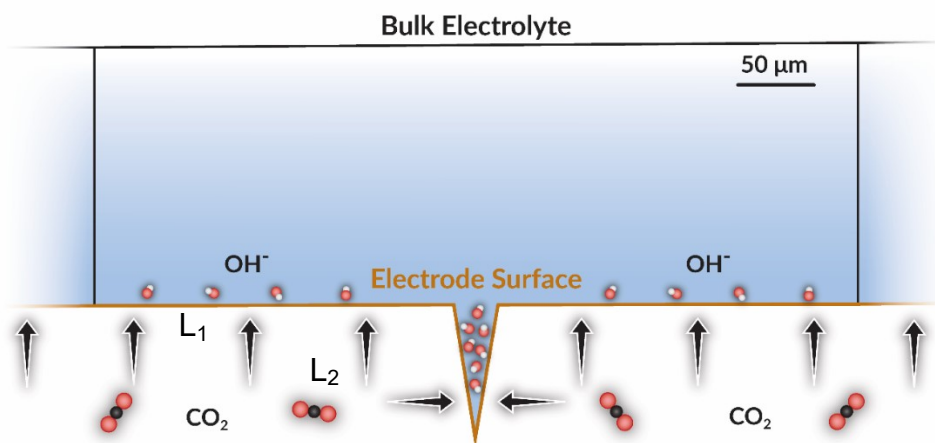


Figure S11: Schematic of the GDE model domain.

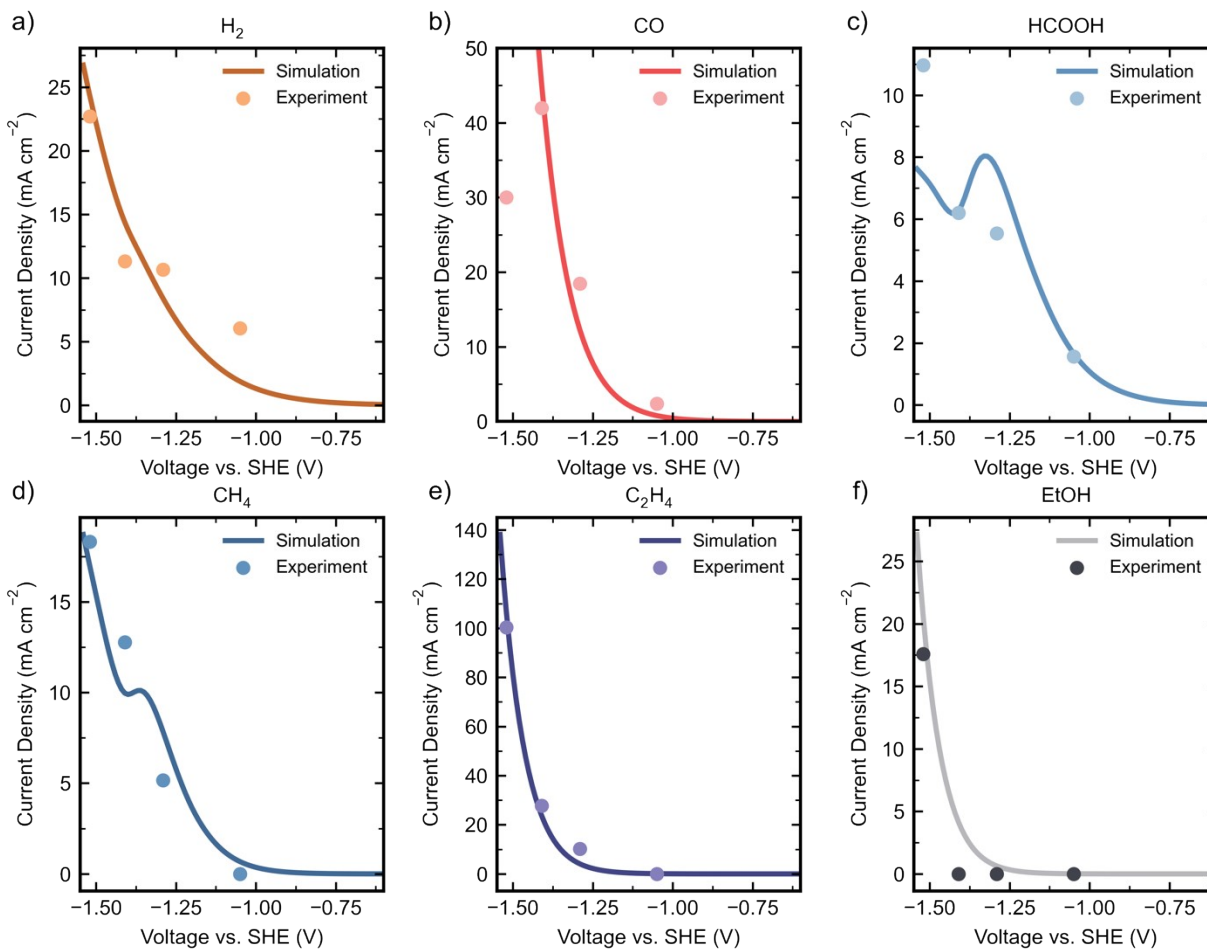


Figure S12: Agreement between experimental (markers) and simulated (solid lines) partial current densities to various hydrocarbon products formed via electrochemical CO₂ reduction on a Cu GDE.

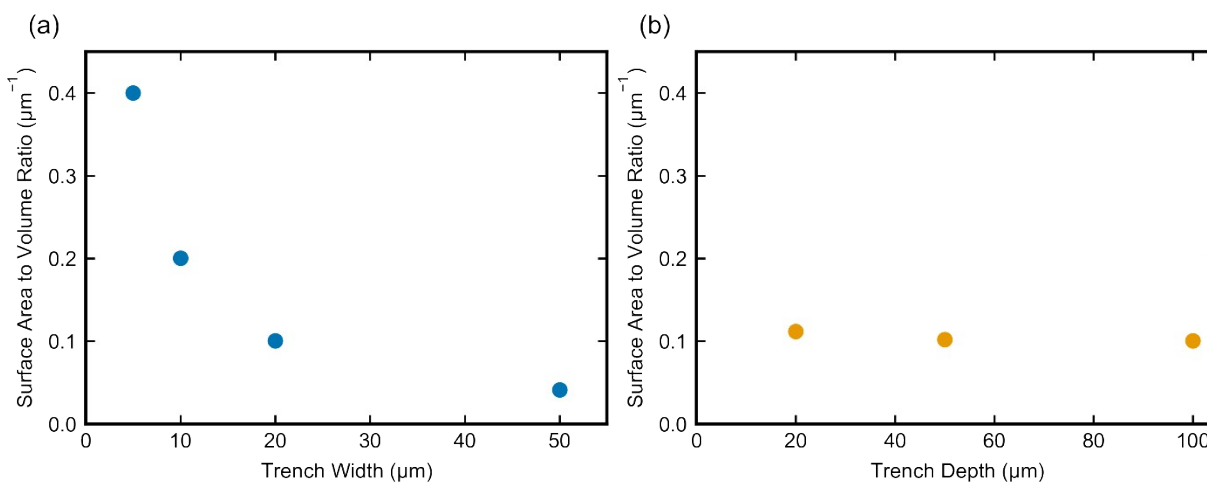


Figure S13: Simulated surface area to volume ratio of trench as a function of (a) trench width at a constant trench depth of 100 μm and (b) trench depth at a constant trench width of 20 μm.

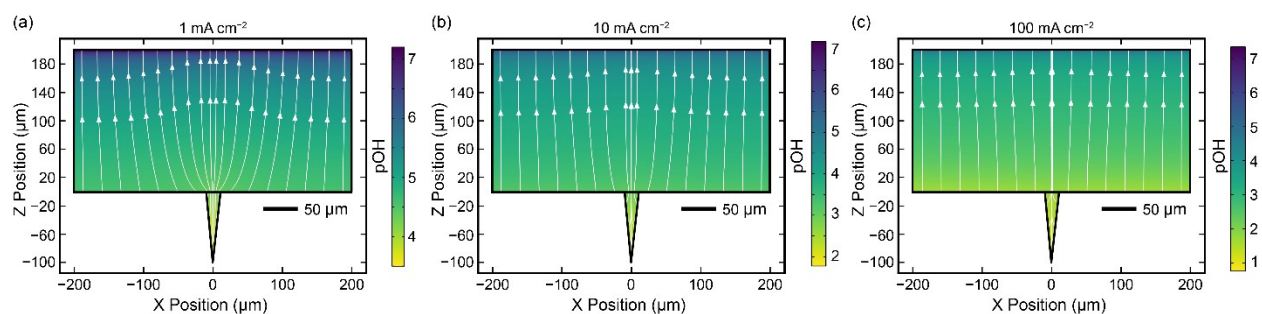


Figure S14: Simulated pOH contour plots over a single, periodic GDE trench in a GDE performing electrochemical CO_2 reduction at total current densities of **(a)** 1, **(b)** 10, and **(c)** 100 mA/cm^2 .

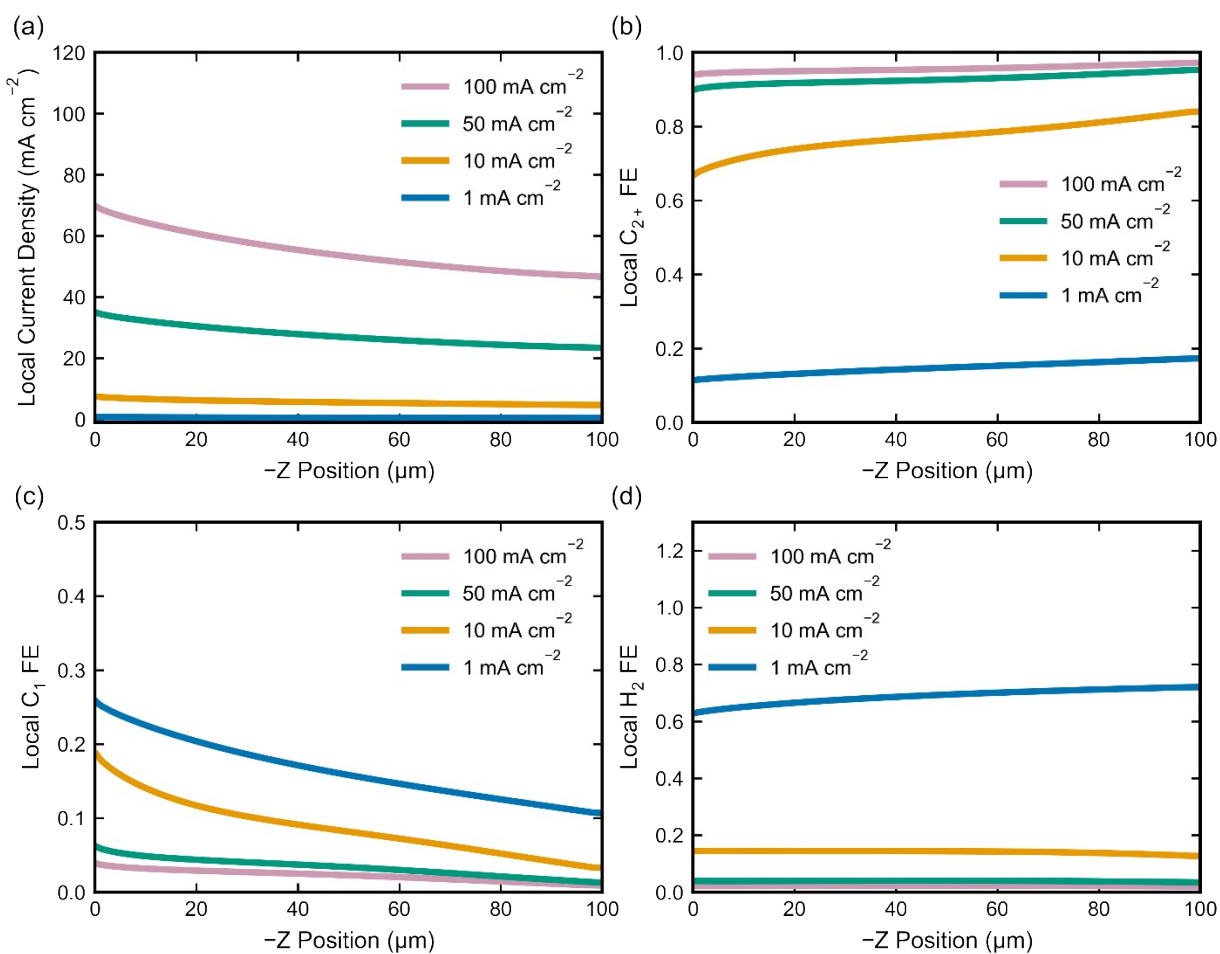


Figure S15: Simulated variation of various performance metrics along the walls of the trench as a function of depth into the trench. $Z = 0 \mu m$ represents the electrode surface or top of the trench, $Z = -100 \mu m$ represents the bottom of the trench. **(a)** Local total current density to all electrochemical reactions on Cu. **(b)** C_{2+} FE along the trench walls. **(c)** C_1 FE along the trench walls. **(d)** H_2 FE along the trench walls. Metrics shown in panels **(a)**-**(d)** are measured at the surface of the trench walls as opposed to averaged within a cross section of the electrolyte, because these metrics are based on current densities to various electrochemical reactions which only occur at the trench walls, and not within the bulk electrolyte.

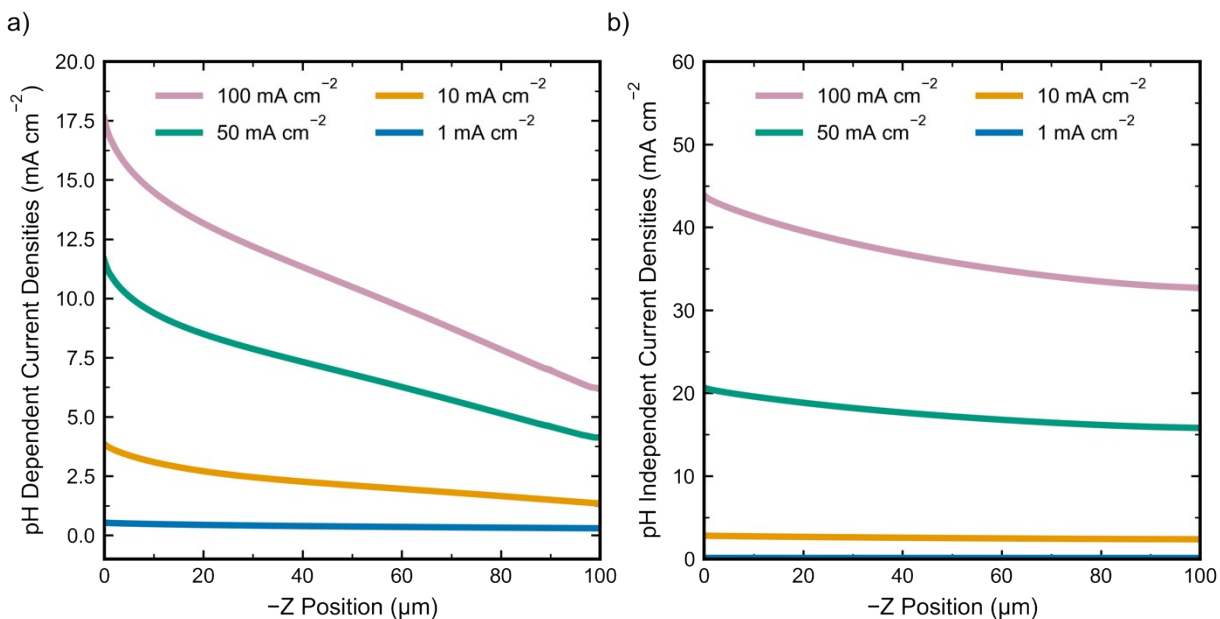


Figure S16: Simulated variation in local partial current density for **(a)** species with pH dependent partial current densities (H_2 , HCOOH , and CH_4), and **(b)** species with pH independent partial current densities (EtOH , C_2H_4 , and CO).

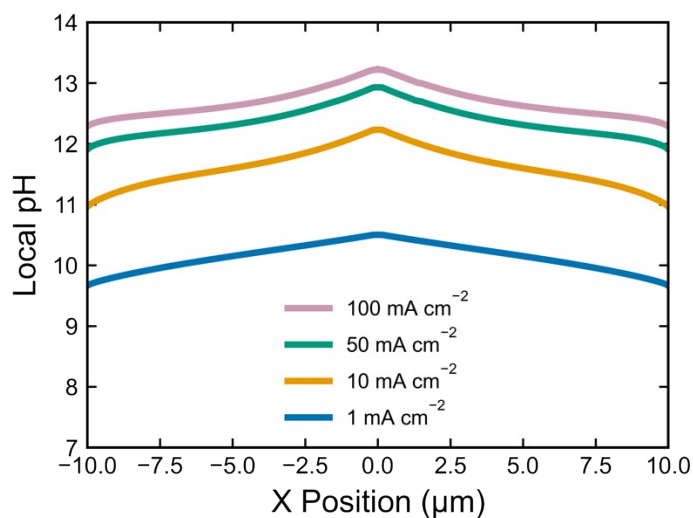


Figure S17: Simulated variation in pH at trench walls as a function of X position. $X = 0$ μm represents the center of the trench. As shown, pH is largest at the center of the trench, where the trench is the deepest due to enhanced OH^- trapping.

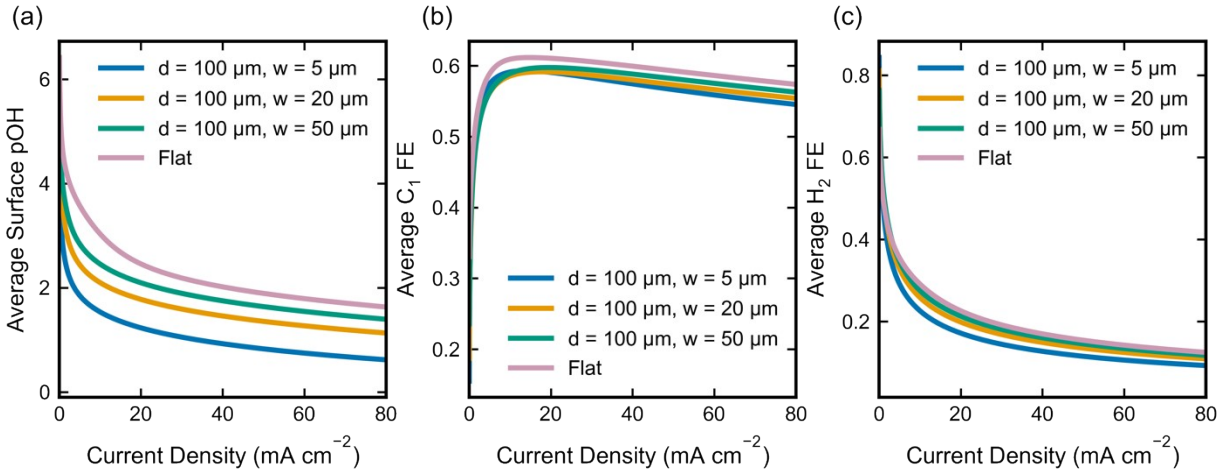


Figure S18: Simulated variation in average (a) pOH, (b) C_1 FE, and (c) H_2 FE as a function of trench width. Current density, pOH, and FEs are averaged across the trench walls.

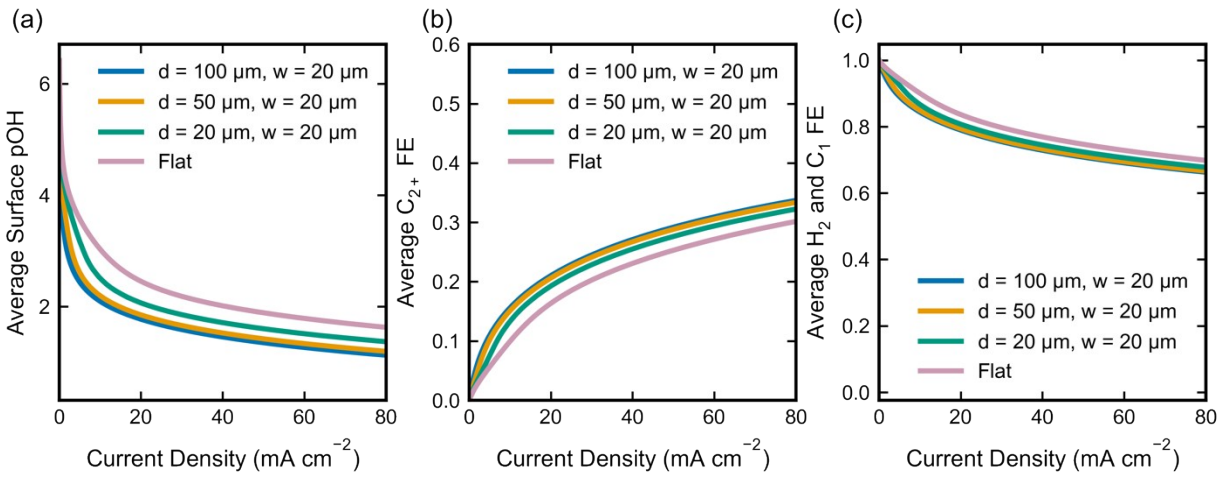


Figure S19: Simulated variation in average (a) pOH, (b) C_2+ FE, and (c) H_2 FE as a function of trench depth. Current density, pOH, and FEs are averaged across the trench walls.

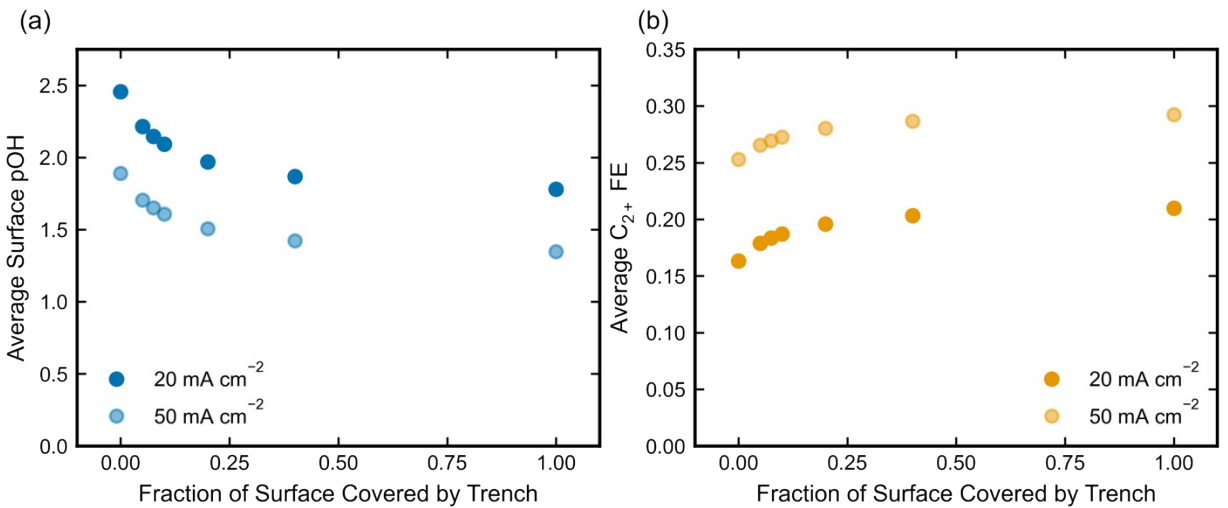


Figure S20: Simulated variation in (a) pOH, and (b) C_{2+} FE at an applied current density of 20 mA/cm² (normalized to ECSA) as a function of the fraction of GDE surface covered by trenches. A current of 20 mA/cm² was chosen due to the increased sensitivity of C_{2+} to pOH at lower current densities. At higher current densities, the C_{2+} FE approaches 1 and is less sensitive to changes in microenvironment. Variation of the surface coverage was achieved by changing the width of the domain (shown schematically in **Figure S11**) from 400 μm to 20 μm, while keeping trench width and depth constant at 20 and 100 μm, respectively. For the zero-coverage case, a rectangular domain with no trench was simulated.

References

- (1) R. Bhide, C. N. Feltenberger, G. S. Phun, G. Barton, D. Fishman, S. Ardo, Quantification of Excited-State Brønsted-Lowry Acidity of Weak Photoacids Using Steady-State Photoluminescence Spectroscopy and a Driving-Force-Dependent Kinetic Theory. *J. Am. Chem. Soc.* 2022, in press, DOI: 10.1021/jacs.2c00554.
- (2) J. Newman, K. E. Thomas-Alyea, *Electrochemical Systems*; Wiley-Interscience, Hoboken, 2004.
- (3) L. C. Weng, A. T. Bell, A. Z. Weber, A Systematic Analysis of Cu-Based Membrane-Electrode Assemblies for CO₂ reduction through Multiphysics Simulation. *Energy Environ. Sci.* 2020, **13** (10), 3592–3606.
- (4) L. C. Weng, A. T. Bell, A. Z. Weber, Towards Membrane-Electrode Assembly Systems for CO₂ Reduction: A Modeling Study. *Energy Environ. Sci.* 2019, **12** (6), 1950–1968.
- (5) J. C. Bui, C. Kim, A. Z. Weber, A. T. Bell, Dynamic Boundary Layer Simulation of Pulsed CO₂ Electrolysis on a Copper Catalyst. *ACS Energy Lett.* 2021, **6**, 1181–1188.
- (6) L. C. Weng, A. T. Bell, A. Z. Weber, Modeling Gas-Diffusion Electrodes for CO₂ Reduction. *Phys. Chem. Chem. Phys.* 2018, **20** (25), 16973–16984.
- (7) K. Williams, N. Corbin, J. Zeng, N. Lazouski, D.-T. Yang, K. Manthiram, Protecting effect of mass transport during electrochemical reduction of oxygenated carbon dioxide feedstocks. *Sustainable Energy Fuels* 2019, **3**, 1225
- (8) J. C. Bui, E. W. Lees, L. M. Pant, I. V. Zenyuk, A. T. Bell, A. Z. Weber, Continuum Modeling of Porous Electrodes for Electrochemical Synthesis. *Chem. Rev.* 2021, *In Review*.
- (9) M. Moradzaman, C. S. Martínez, G. Mul, Effect of Partial Pressure on Product Selectivity in Cu-Catalyzed Electrochemical Reduction of CO₂. *Sustain. Energy Fuels* 2020, **4** (10), 5195–5202.
- (10) L. Wang, S. A. Nitopi, E. Bertheussen, M. Orazov, C. G. Morales-Guio, X. Liu, D. C. Higgins, K. Chan, J. K. Nørskov, C. Hahn, T. F. Jaramillo, Electrochemical Carbon Monoxide Reduction on Polycrystalline Copper: Effects of Potential, Pressure, and pH on Selectivity toward Multicarbon and Oxygenated Products. *ACS Catal.* 2018, **8** (8), 7445–7454.
- (11) L.-C. Weng, A. T. Bell, A. Z. Weber, A Systematic Analysis of Cu-Based Membrane- Electrode Assemblies for CO₂ Reduction through Multiphysics Simulation. *Energy Environ. Sci.* 2020, **13**, 3592-3606.
- (12) X. Liu, P. Schlexer, J. Xiao, Y. Ji, L. Wang, R. B. Sandberg, M. Tang, K. S. Brown, H. Peng, S. Ringe, C. Hahn, T. F. Jaramillo, J. K. Nørskov, K. Chan, pH Effects on the Electrochemical Reduction of CO₍₂₎ towards C₂ Products on Stepped Copper. *Nat. Commun.* 2019, **10** (1), 1–10.
- (13) A. S. Varela, M. Kroschel, T. Reier, P. Strasser, Controlling the selectivity of CO₂ electroreduction on copper: The effect of the electrolyte concentration and the importance of the local pH. *Catalysis Today* 2016, **260**, 8-13

- (14) G. Kastlunger, L. Wang, N. Govindajaran, H. H. Heenen, S. Ringe, T. Jaramillo, C. Hahn, K. Chan, Using pH Dependence to Understand Mechanisms in Electrochemical CO₂ Reduction. *ACS Catal.* 2022, **12**, 8, 4344-4357
- (15) E. W. Lees, A. Liu, J. C. Bui, S. Ren, A. Z. Weber, C. P. Berlinguette, Electrolytic Methane Production from Reactive Carbon Solutions. *ACS Energy Lett.* 2022, **7**, 5, 1712-1718
- (16) R. E. Vos, M. T. M. Koper, The Effect of Temperature on the Cation Promoted Electrochemical CO₂ Reduction on Gold. *ChemElectroChem* 2022, **9**, 13
- (17) S. Ringe, E. L. Clark, J. Resasco, A. Walton, B. Seger, A.-T. Bell, K. Chan, Understanding Cation Effects in Electrochemical CO₂ Reduction. *Energy Environ. Sci.* 2019, **12** (10), 3001–3014.
- (18) C. Kim, L.-C. Weng, A. T. Bell, The Impact of Pulsed Electrochemical Reduction of CO₂ on the Formation of C₂₊ Products over Cu. *ACS Catal.* 2020, **10**, 21, 12403-12413.